

Article

Metal Substitution versus Oxygen-Storage Modifier to Regulate the Oxygen Redox Reactions in Sodium-Deficient Three-Layered Oxides

Mariya Kalapsazova, Rositsa Kukeva, Ekaterina Zhecheva and Radostina Stoyanova * 

Institute of General and Inorganic Chemistry, Bulgarian Academy of Sciences, 1113 Sofia, Bulgaria; maria_l_k@svr.igic.bas.bg (M.K.); rositsakukeva@yahoo.com (R.K.); zhecheva@svr.igic.bas.bg (E.Z.)

* Correspondence: radstoy@svr.igic.bas.bg; Tel.: +359-2-9793915

Abstract: Sodium-deficient nickel-manganese oxides with three-layered stacking exhibit the unique property of dual nickel-oxygen redox activity, which allows them to achieve enormous specific capacity. The challenge is how to stabilize the oxygen redox activity during cycling. This study demonstrates that oxygen redox activity of $P3\text{-Na}_{2/3}\text{Ni}_{1/2}\text{Mn}_{1/2}\text{O}_2$ during both Na^+ and Li^+ intercalation can be regulated by the design of oxide architecture that includes target metal substituents (such as Mg^{2+} and Ti^{4+}) and oxygen storage modifiers (such as CeO_2). Although the substitution for nickel with Ti^{4+} amplifies the oxygen redox activity and intensifies the interaction of oxides with NaPF_6 - and LiPF_6 -based electrolytes, the Mg^{2+} substituents influence mainly the nickel redox activity and suppress the deposition of electrolyte decomposed products (such as MnF_2). The CeO_2 -modifier has a much stronger effect on the oxygen redox activity than that of metal substituents; thus, the highest specific capacity is attained. In addition, the CeO_2 -modifier tunes the electrode–electrode interaction by eliminating the deposition of MnF_2 . As a result, the Mg -substituted oxide modified with CeO_2 displays high capacity, excellent cycling stability and exceptional rate capability when used as cathode in Na-ion cell, while in Li-ion cell, the best performance is achieved for Ti-substituted oxide modified by CeO_2 .

Keywords: layered oxides; EPR spectroscopy; oxygen redox activity; cerium dioxide; metal substitution; sodium-ion batteries; lithium-ion batteries



Citation: Kalapsazova, M.; Kukeva, R.; Zhecheva, E.; Stoyanova, R. Metal Substitution versus Oxygen-Storage Modifier to Regulate the Oxygen Redox Reactions in Sodium-Deficient Three-Layered Oxides. *Batteries* **2022**, *8*, 56. <https://doi.org/10.3390/batteries8060056>

Academic Editors: Emma Kendrick, Lin Chen and Brj Kishore

Received: 7 May 2022

Accepted: 8 June 2022

Published: 15 June 2022

Publisher's Note: MDPI stays neutral with regard to jurisdictional claims in published maps and institutional affiliations.



Copyright: © 2022 by the authors. Licensee MDPI, Basel, Switzerland. This article is an open access article distributed under the terms and conditions of the Creative Commons Attribution (CC BY) license (<https://creativecommons.org/licenses/by/4.0/>).

1. Introduction

The transition to large-scale energy storage is dictated by the invention of more powerful, safer and cheaper batteries dictates [1]. These batteries are designed to replace the widely-used today lithium-ion batteries (LiIBs) without changing the mechanism of battery operation [2]. Nowadays, the most competitive alternatives of LiIBs are sodium-ion batteries (NaIBs) [3]. Both Li- and Na-batteries store energy by intercalation reactions occurring in the bulk of electrodes [2,3]. The intercalation reactions ensure excellent reversibility, but the specific capacity is limited by the redox properties of cationic constituents (such as transition metal ions Ni, Co, etc.) in the crystal structure of electrode materials [2]. This limitation can effectively be overcome if the redox activities of cationic and anionic constituents are unlocked simultaneously [4].

The unique property of dual redox activity of transition metal ions and lattice oxygen has been established for both the lithium and sodium transition metal oxides (i.e., LiTMOs and NaTMOs) [4,5]. Furthermore, this property is insensitive to the manner of layer stacking: for LiTMOs, the three-layer stacking is the stable structural configuration (i.e., O3-type), while for NaTMOs, both two- and three-layer stacking are observed (i.e., P2 and P3-types) [6]. Notwithstanding the common features of both oxides, the driving force for the activation of oxygen redox activity is different: for LiTMOs, the availability of even small amounts of Li ions in transition metal layers serves as a key trigger in the activation

of oxygen redox reaction [7,8], while, for NaTMOs, the metal substitution at Mn^{4+} -sites with mono-, bi- and four-valent ions (such as Li^+ [9], Ni^{2+} [10], Mg^{2+} [11], Zn^{2+} [12], Cu^{2+} [13], Ti^{4+} [14], etc.), as well as the creation of vacancies in transition metal layers [15], is responsible for the oxygen redox activity. The common drawbacks for both LiTMOs and NaTMOs are the poor reversibility of the electrochemical reaction and the quick capacity fade during cycling [16]. The weak electrochemical features are a consequence of the electrochemically generated over-oxidized oxygen that leads to a destabilization of the layered structure and to an enhancement of the surface reactivity towards the acidic liquid electrolytes [15,17]. That is why the recent research efforts are mainly directed at the stabilization of lattice oxygen during the redox reaction.

There are several approaches for the stabilization of lattice oxygen that can be differentiated with respect to the manner of electrode modification. Concerning the oxide bulk, the reversible oxygen redox reactions in LiTMOs can be facilitated when the lattice oxygen is selectively replaced by fluorine or when the cations are disordered across transition metal and lithium layers [18,19]. The fluorination of LiTMOs affects not only the lattice oxygen but also evokes suppression in the irreversible gas release and surface reactions [18]. The co-doping of NaTMOs with lithium and titanium gives rise to the stabilization of lattice oxygen and to an enhancement of reversibility at oxygen redox reactions [20]. The surface coating of LiTMOs and NaTMOs is a common approach to inhibit, on one hand, the oxygen loss during the electrochemical reaction and, on the other, to suppress the side reactions between the electrode and the electrolyte [21–23]. The most used surface coatings are Al_2O_3 , AlF_3 , $AlPO_4$, MgO , TiO_2 and Li_2TiO_3 [24–26]. Instead of metal oxides, surface decoration with an aim to stabilize underbonded oxidized O species in near-surface regions of oxides completely depleted of alkali ions is also used [27]. Thus, the sulfur deposition on Li-rich layered oxides is another approach that permits turning the under-coordinated surface oxygen into sulfate groups SO_4^{2-} , thus depressing gas release and side reactions with the electrolyte [28]. To intensify the effect on the oxygen redox activity, a strategy including simultaneous doping and coating is also applied for both LiTMOs and NaTMOs [21,29]. The next strategy for depressing the oxygen evolution from LiTMOs is through surface doping with highly oxidized ions, such as Os, Sb, Ru, Ir, or Ta, which are prone to segregate on the oxide surface [30]. Recently, we have proposed a new concept for the stabilization of lattice oxygen in NaTMOs [31]. This concept comprises using oxygen-storage materials that serve as a buffer that accumulates the evolved oxygen during the complete alkali ion extraction from the layered oxide, and, during the reverse reaction, the accumulated oxygen will be returned to the layered oxide [30]. The concept is demonstrated in the case of three-layered sodium nickel manganese oxide $P3-Na_{2/3}Ni_{1/2}Mn_{1/2}O_2$. When the layered oxide is treated with an oxygen storage material, such as CeO_2 , there is a drastic increase in the reversible capacity during both the single intercalation of Na^+ or Li^+ and co-intercalation of Li^+ and Na^+ [30]. Based on the above findings, one can conclude that there is no unified concept of how to stabilize the lattice oxygen during the electrochemical reaction. That is why the rational manipulating of different factors that stabilize or destabilize the lattice oxygen will help to reveal the full potential of high-capacity oxide electrodes.

Herein, we unveil the interplay between metal substitution, treatment with oxygen storage materials and anionic redox activity in sodium nickel manganese oxides with three-layer stacking ($P3-Na_{2/3}Ni_{1/2}Mn_{1/2}O_2$) during single Na^+ and Li^+ intercalation. As metal substituents, Mg^{2+} and Ti^{4+} ions were used. The Mg^{2+} ions are selected since they induce reversible oxygen redox activity irrespective of the layered stacking ($P2$ and $P3$ -modifications) [27,32,33], and they also allow avoiding the oxygen loss during the charging of the $P2$ phase at high potentials [27]. In comparison with Mg^{2+} , the effect of Ti^{4+} ions on the oxygen redox activity is not so clear, but it is accepted that Ti^{4+} stabilizes the oxygen environment by strengthening the bonding between metal and oxygen and by decreasing the local ordering of transition metal ions [14,34]. In this study, the nominal composition of metal-substituted oxides is $P3-Na_{2/3}Ni_{1/3}Mg_{1/6}Mn_{1/2}O_2$ and $P3-Na_{2/3}Ni_{1/3}Ti_{1/6}Mn_{1/2}O_2$. Furthermore, the metal-substituted oxides are treated with an oxygen storage material,

such as CeO₂, which has been shown to have a dramatic effect on the performance of unsubstituted P3-Na_{2/3}Ni_{1/2}Mn_{1/2}O₂ [31]. The oxide architecture including metal substitution and oxygen-storage treatment allows achieving high capacity and improved cycling stability when electrode materials operate in Li- and Na-ion batteries.

2. Results and Discussions

2.1. Structure of Metal-Substituted and CeO₂-Treated Oxides

The addition of Mg and Ti to P3-Na_{2/3}Ni_{1/2}Mn_{1/2}O₂ proceeds in the framework of the layered structure, where the manner of layer stacking and Na coordination are preserved (Figure S1). The lattice parameters are listed in Table 1. Although the Mg-substituted oxide exhibits unchanged lattice parameters, the incorporation of titanium into the layered oxide provokes a slight lattice expansion. The observed lattice dependences are related to the selective replacement of Ni²⁺ or Ni³⁺ ions in P3-Na_{2/3}Ni_{1/2}Mn_{1/2}O₂ by two-valent Mg²⁺ and four-valent Ti⁴⁺ ions. For the unsubstituted oxide P3-Na_{2/3}Ni_{1/2}Mn_{1/2}O₂, the charges of Na⁺ are compensated at the expense of the Ni ions (i.e., they adopt simultaneously the oxidation states of +2 and +3), while manganese ions are stabilized in an oxidation state of +4. [31,35]. The insertion of Mg²⁺ into P3-Na_{2/3}Ni_{1/2}Mn_{1/2}O₂ is accomplished through the replacement of Ni²⁺, which has an ionic radius close to that of Mg²⁺ (0.70 versus 0.72 Å). Contrary to Mg²⁺, the incorporation of Ti⁴⁺ ions takes place by replacing smaller, highly oxidized Ni ions (0.57 Å for Ni³⁺ versus 0.605 Å for Ti⁴⁺), thus leading to lattice expansion. However, the partial replacement of Mn⁴⁺ by Ti⁴⁺ cannot be rejected. Thus, the most possible structural formulas for Mg- and Ti-substituted oxides are Na_{2/3}[Ni³⁺_{1/3}Mg²⁺_{1/6}Mn⁴⁺_{1/2}]O₂ and Na_{2/3}[Ni²⁺_{1/3}Ti⁴⁺_{1/6}Mn⁴⁺_{1/2}]O₂.

Table 1. Lattice parameters for Na_{2/3}Ni_{1/2}Mn_{1/2}O₂, Na_{2/3}Ni_{1/3}Mg_{1/6}Mn_{1/2}O₂, Na_{2/3}Ni_{1/3}Ti_{1/6}Mn_{1/2}O₂ and their CeO₂-treated analogues.

Samples	$a \pm 0.0001, \text{Å}$	$c \pm 0.002, \text{Å}$	$V \pm 0.02, \text{Å}^3$
NNM	2.8867	16.7692	121.01
NM16	2.8889	16.7789	121.27
NT16	2.8992	16.8237	122.46
CNNM	2.8872	16.7724	121.09
CNM16	2.8867	16.7732	121.29
CNT16	2.8889	16.8236	122.54

The impregnation of metal-substituted oxides with cerium acetate, followed by thermal treatment at 700 °C, yields two-phase composites between layered oxides and CeO₂ (Figure S1). The lattice parameters of the metal-substituted oxides in the composites remain intact, which indicates that the oxide bulk is free of any cerium ions (Table 1). This is valid for all samples, irrespective of the metal substituents.

To go inside the structure of metal-substituted and CeO₂-treated oxides, an EPR spectroscopy is undertaken. Irrespective of the modification way, all oxides display a single line with a Lorentzian shape and a g -factor of 2.0. The main feature of the EPR signal is its strong temperature dependence: going from 300 to 100 K, the g -factor decreases together with line narrowing (Figure 1). This signal behavior reflects the exchange interactions between nickel and manganese ions inside the transition metal layers, as was previously established for the untreated P3-Na_{2/3}Ni_{1/2}Mn_{1/2}O₂ [33,36]. Given that Mg²⁺ and Ti⁴⁺ ions are diamagnetic and they substitute for paramagnetic nickel ions, one could expect different temperature dependencies of the g -factor and EPR line width for metal-substituted oxides. As can be expected, the Mg²⁺-substituted oxide possesses a g -factor that decreases more slowly on cooling in comparison with that of the unsubstituted oxide. In synchrony with the g -factor, the EPR line width is narrower in the whole temperature range between 300 and 100 K. This EPR signal behavior is consistent with the selective replacement of paramagnetic Ni²⁺ with diamagnetic Mg²⁺ ions, increasing the relative part of the Mn⁴⁺ ions. Contrary to the interactions between nickel and manganese ions, the exchange interactions between

identical Mn^{4+} ions produce a narrower EPR signal with a g -factor independent of the registration temperature. For the sake of comparison, the EPR parameters of exchanged coupled Mn^{4+} ions in two-layer sodium manganese oxide (i.e., $\text{P2-Na}_{2/3}\text{MnO}_2$) are $g = 1.99$ and a line width of around 90 mT [31,37].

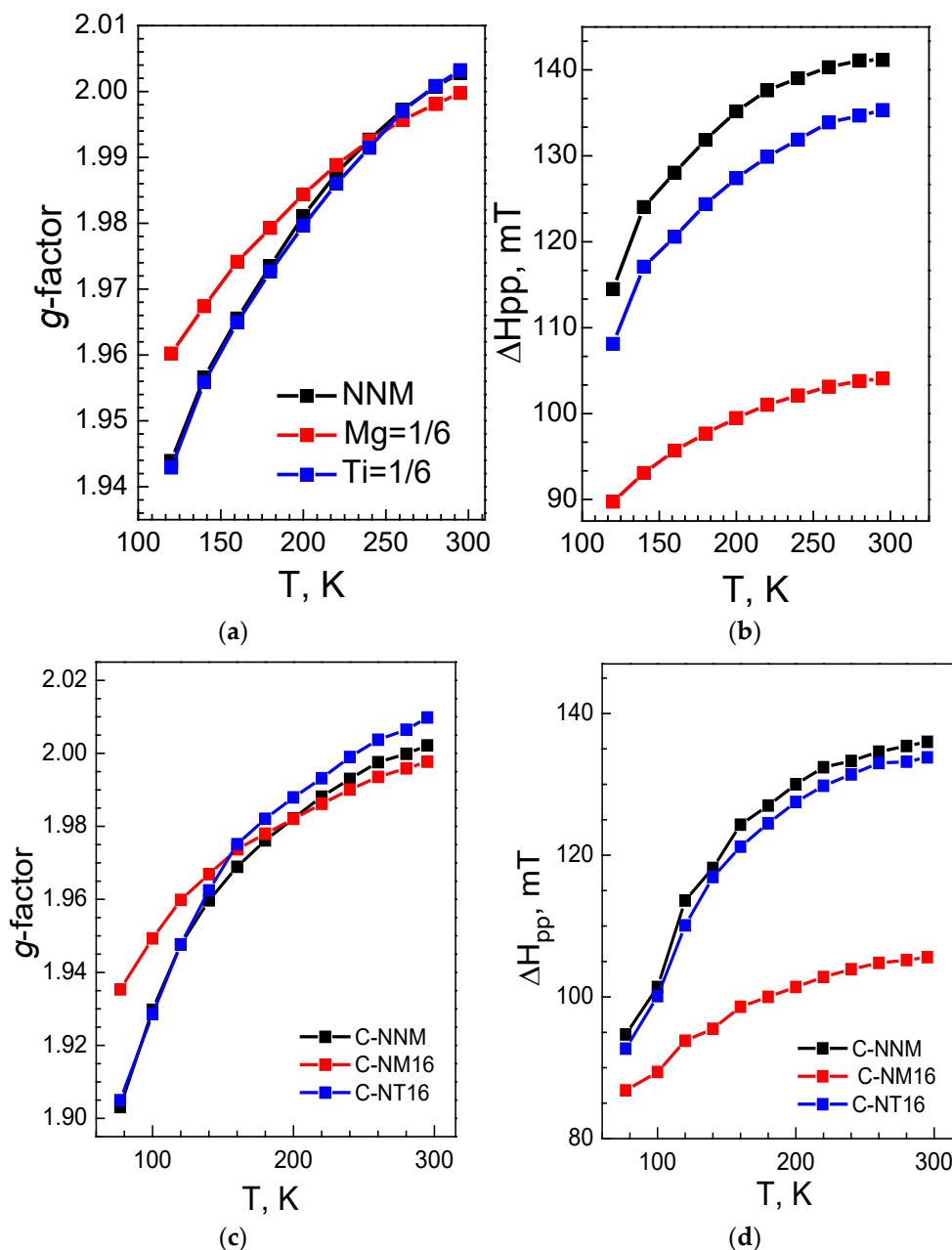


Figure 1. Temperature dependence of the g -factor and EPR line width (ΔH_{pp}) of NNM, NM16, NT16 (a,b) and their CeO_2 -treated analogues (c,d).

Irrespective of the diamagnetic character, Ti^{4+} ions have a slight impact on the temperature dependence of both the g -factor and the EPR line width. The lack of significant dependence implies that Ti^{4+} ions provoke only slight changes in the ratio between paramagnetic nickel and manganese ions. This can be interpreted that Ti^{4+} ions substitute not only for nickel ions but also for manganese ions. However, these data do not allow quantifying the exact part of Ti that substitutes for Ni or Mn. Based on XRD and EPR data, one can conclude that highly oxidized Ni ions are dominant in Mg-substituted oxide, while in Ti-substituted oxide, low-oxidized Ni ions prevail.

The treatment of metal-substituted oxides with CeO_2 does not induce any changes in the EPR parameters of the unmodified oxides (Figure 1). This evidences that the layered structure of metal-substituted oxides is free from cerium ions. On the other hand, the EPR data support once again that heating the impregnated oxide with cerium acetate enables obtaining two-phase composites between layered oxide and CeO_2 .

The next important characteristic of substituted and treated oxides is their morphology (Figure 2). All oxides display a morphology consisting of micro-metric aggregates, which are composed of nano-sized primary particles. The primary particles vary in size between 10 and 200 nm, and the most inhomogeneous particle distribution is observed for NNM. After treatment of NNM with CeO_2 , there is strong shrinkage in the particle sizes' distribution with a center of gravity of around 10–40 nm. This trend is obeyed for CNM16, while for CNT16, it is not well pronounced. The common morphological features demonstrate that CeO_2 modifies layered oxides in the same manner— CeO_2 seems to suppress the particle aggregation.

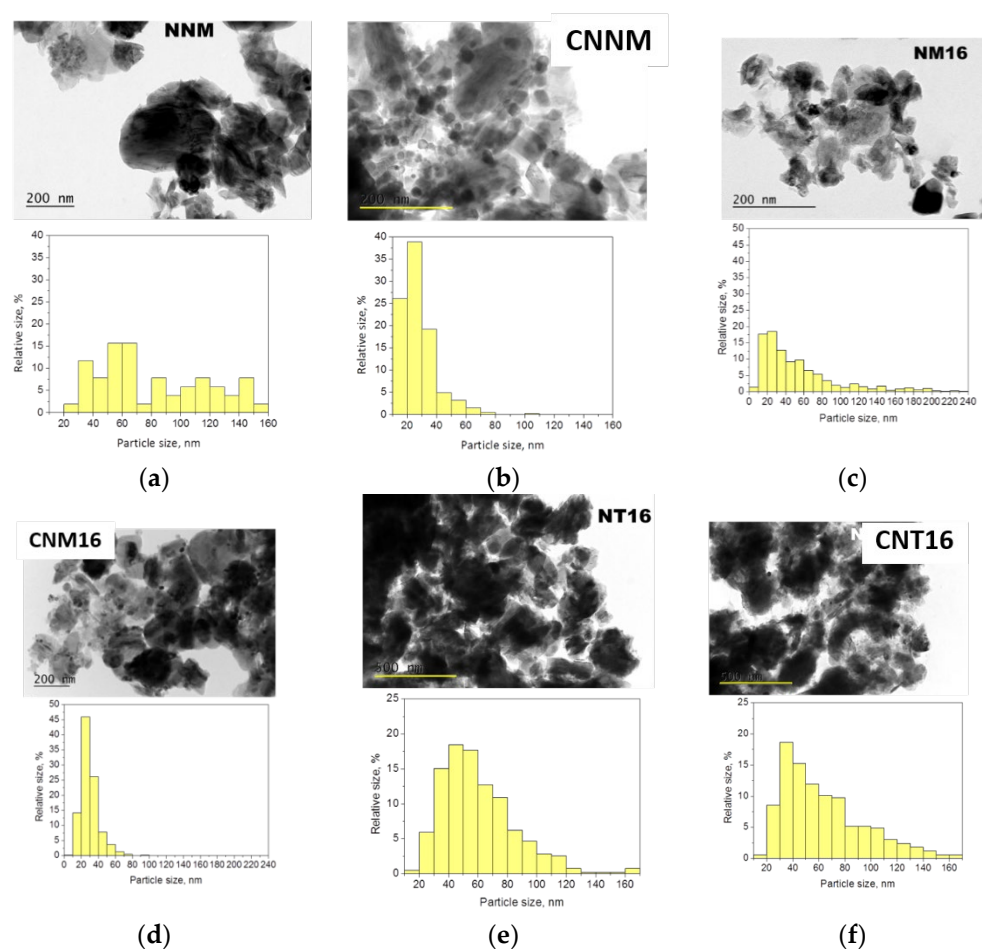


Figure 2. Bright-field TEM images and corresponding particle size–distribution curves for NNM, NM16, NT16 (a–c) and their CeO_2 -treated analogues (CNNM, CNM16 and CNT16) (d–f).

Irrespective of the treatment type, the HR-TEM images display that, for all the samples, primary nanoparticles retain their good crystallinity (Figure 3). When layered oxides are modified with CeO_2 , lattice fringes are observed due to two phases. This means that, in modified oxides, there is intimate contact between particles of the two phases, which is developed at a nano-scale range (Figure 3).

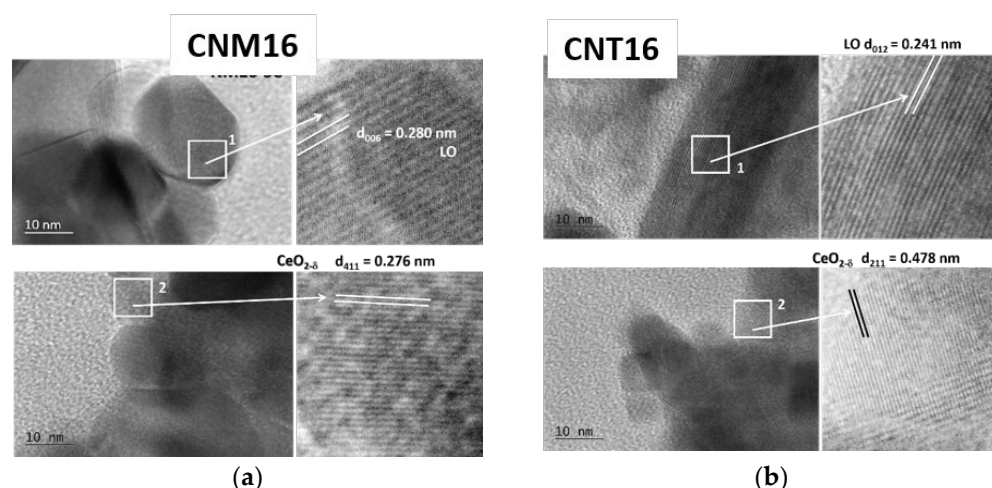


Figure 3. HR-TEM images of CNM16 (a) and CNT16 (b). The lattice fringes from the layered oxide (LO) and $\text{CeO}_{2-\delta}$ are indicated.

2.2. Electrochemical Behavior of Metal-Substituted and CeO_2 -Treated Oxides

2.2.1. Sodium-Ion Cells

Metal-substituted oxides. The contribution of Mg^{2+} and Ti^{4+} to the electrochemical properties of NNM is monitored by CV (Figure 4). At first glance, the CV curves display similar profiles for all the samples. A close inspection, however, enables distinguishing some peculiarities.

The open circuit voltage (OCV) of cells increases from Ti- to Mg-substituted electrodes via unsubstituted NNM (Figure 3). Given that Mg^{2+} and Ti^{4+} ions are electrochemically inactive, this order reflects the oxidation state of nickel ions: the higher the Ni oxidation state, the higher OCV is. Thus, the observed increase in the OCV coincides with the structural data, according to which low-oxidized Ni ions are stabilized after Ti^{4+} substitution, while highly oxidized Ni ions appear after Mg^{2+} -substitution, respectively.

After the first anodic scan, there are two intensive peaks in the 3V-range, whose positions are insensitive to the kind of metal substituents (i.e., peaks at 3.5 and 3.8 V, respectively). For the Mg-substituted oxide, an additional peak at 4.0 V superimposed on the main peak at 3.8 V appears. In the 4.0 V range, there are also two peaks: one at 4.4 V and the other above 4.7 V. The peak at 4.4 V is visible for all the samples, and it is most clearly pronounced for NT-16, while the peak above 4.7 V depends on the kind of metal substituents. The Mg^{2+} substituents shift the peak from 4.7 to 4.9 V, while the Ti^{4+} substituents significantly suppress this peak.

After the reverse cathodic scan process, four peaks grow in intensity, three of them being insensitive to the metal substituents at 3.4 V, 3.1 V and 3.4 V. The last peak at 3.9 V seems similar for NNM and NT-16, while for NM-16, this peak appears at a lower potential of 3.6 V.

The cycling entails a significant change in high-voltage peaks. The anodic peak at potentials above 4.7 V disappears after the first scan. The anodic and cathodic peaks at 4.4 V and 3.9 V are broadening and are shifting to lower potentials upon cycling—this being more significant for the Mg-substituted oxide. The redox peaks at the potentials of (3.5 V–3.8 V)/(3.2 V–3.5 V), as well as the low-voltage peak at 2.2/1.8 V, remain intact upon cycling. The stable curve profile is achieved after five cycles.

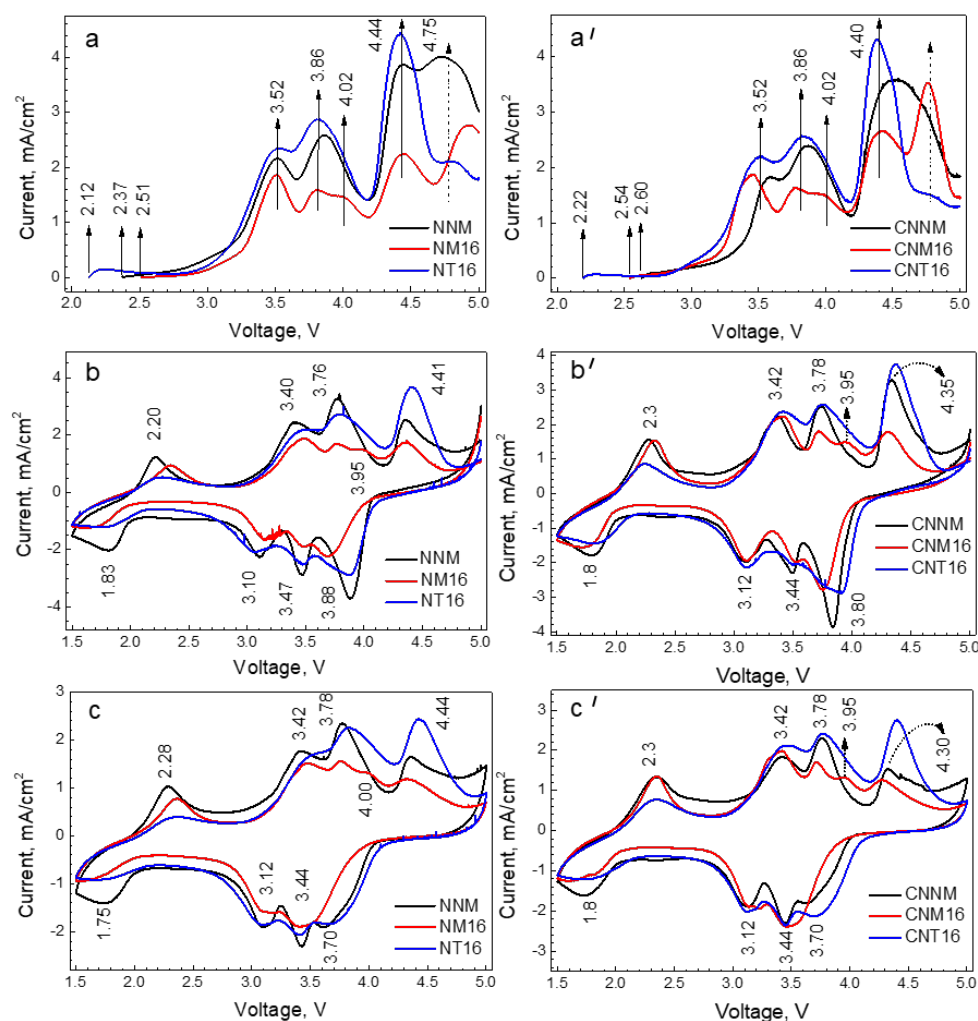


Figure 4. CV curves of metal-substituted oxides (a–c) and their CeO₂-treated analogues (a'–c') in sodium-ion cells: (i) first anodic scan (a,a'); (ii) the corresponding cathodic scan and next anodic scan (b,b'); (iii) CV curves after five cycle (c,c'). The scan rate is 1 mV/s.

Based on our previous study on $P3\text{-Na}_{2/3}\text{Ni}_{1/2}\text{Mn}_{1/2}\text{O}_2$, the redox peaks in the range of 3.2–3.8 V are due to the partial sodium extraction/insertion inducing a reversible monoclinic distortion of the layered structure [35,38]. The sodium charges are compensated through the redox activity of nickel ions (i.e., $\text{Ni}^{2+}/\text{Ni}^{3+}/\text{Ni}^{4+}$). The comparison of the CV curve profiles discloses that Ti^{4+} substituents do not influence the reaction of partial Na-extraction/insertion from/into the layered structure, while Mg^{2+} substituents have a slight impact manifesting as the appearance of an additional peak at 3.9 V. Between 4.2 and 4.5 V, the complete extraction of Na^+ is achieved, which yields a restoration of the crystal structure [33,38]. In this voltage range, both nickel ions and lattice oxygen are involved in the electrochemical reaction. Among metal substituents, it appears that Ti^{4+} ions amplify the peak associated with nickel and oxygen redox activity. Because of the irreversibility of the anodic peak above 4.7 V, it can be attributed to a side reaction of electrolyte decomposition initiated by interaction with the oxide electrode. It is interesting that this process takes place easily at unsubstituted oxide. For Mg-substituted oxide, the electrolyte decomposition begins at higher potentials, while at the Ti-substituted oxide, this reaction is suppressed.

To outline the effect of metal substituents on the cationic and oxygen redox activity, Figure 5 compares the specific capacity delivered by NNM, NM-16 and NT-16 in two voltage ranges: in the limited voltage range of 2.0 V–4.2 V, where cations are only redox active, and in the extended voltage range of 2.0–4.3 V, where the oxygen redox activity is

unlocked. The voltage ranges are selected in a way to avoid electrolyte decomposition. For the sake of convenience, the charge–discharge curves for metal-substituted oxides are given in Figure 5. Figure 4 shows the corresponding cycling stability and rate capability of oxides. In the limited voltage range, the specific capacity and cycling stability are comparable for all the samples. Even in this case, the Mg-substituted oxide displays a better rate capability in comparison with NNM and NT-16. This observation can be associated with a slight impact of the Mg^{2+} substituents on the reaction of partial Na-extraction/insertion (Figure 4).

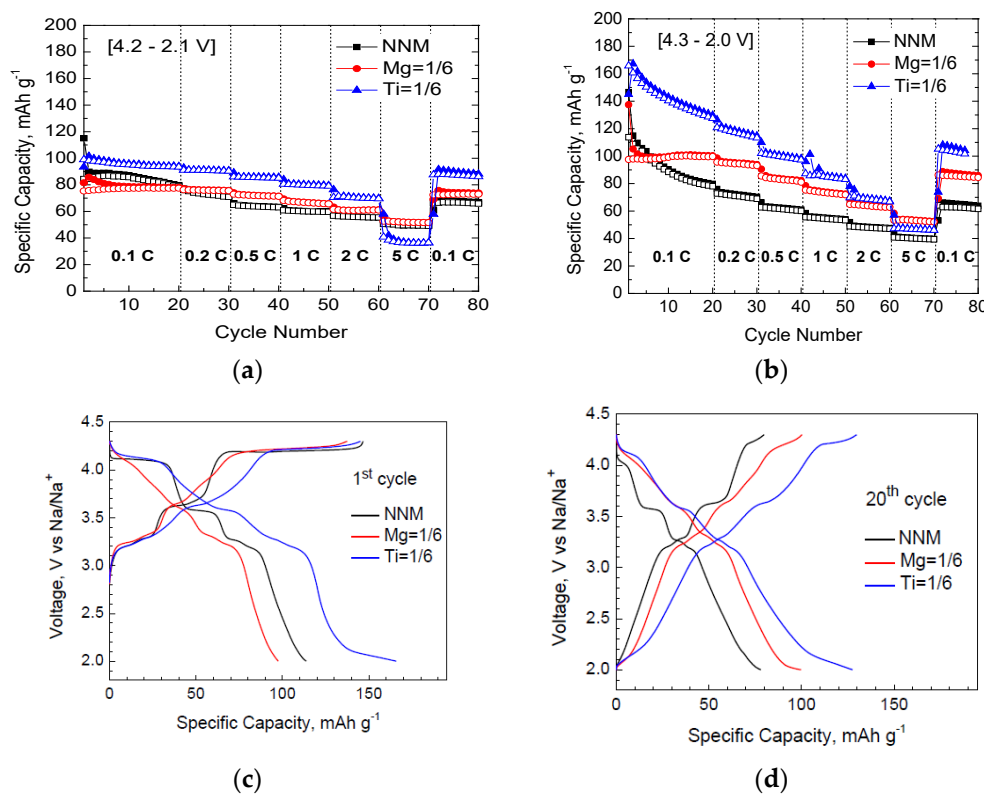


Figure 5. Specific capacity, cycling stability and rate capability for NNM, NM16 and NT16 in sodium-ion cells cycled in two voltage windows: (a)—[4.2–2.1] V and (b)—[4.3–2.0] V. Charge–discharge curves after the 1st (c) and 20th (d) cycles for NNM, NM16 and NT16 in sodium-ion cells.

In contrast, in the extended voltage range, the Ti-substituted oxide delivers the highest capacity (i.e., around 170 mAh/g) with moderate cycling stability (i.e., around 78% at C/10) and poorest rate capability (i.e., the capacity loss more than three times going from C/10 to 5C) (Figure 5). The Mg-substituted oxide is characterized by the lowest specific capacity (i.e., around 100 mAh/g), but it outperforms the other oxides in respect of the cycling stability (i.e., around 100%) and rate capability (i.e., the capacity loss less than two times going from C/10 to 5C). The unsubstituted oxide demonstrates the weakest performance in comparison with NM-16 and NT-16. The electrochemical results reveal that Ti⁴⁺ substituents amplify the oxygen redox activity of the layered oxide (Figures 4 and 5), which could be correlated with the stabilization of low-oxidized nickel ions in Ti-containing oxides (Figure 2). In comparison with Ti⁴⁺, the Mg^{2+} substituents have an impact on the nickel redox activity before the activation of the oxygen redox reaction, thus contributing to the excellent cycling stability and rate capability of the layered oxides. The electrochemical impact of the Mg^{2+} substituents could be related to their aptitude to stabilize highly oxidized Ni ions in the layered oxide.

CeO₂-treated oxides. After the oxide treatment with CeO₂, the main features of the CV curves are preserved (Figure 4). The OCV increases from Ti- to Mg-substituted oxides. The redox peaks at (3.5 V–3.8 V)/(3.2 V–3.5 V) are similar for all the treated oxides. For CNM16, the low-intensive peak at 4.0 V is superimposed on the main anodic peak at 3.8 V, as in

the case of the untreated oxides. The main difference between metal-substituted oxides and their CeO_2 -treated analogues is related to the peaks appearing in the 4.0 V region. The CeO_2 additives amplify the redox peak at 4.4 V/3.9 V, and this peak is still visible after five cycles, especially for the Mg-substituted oxide. The irreversible anodic peak at 4.7 V seems to shift towards lower potentials for CNNM and CNM16 and remains hardly visible for CNT16, as was established for untreated NT16. This means that CeO_2 has an impact on both the oxygen redox activity and the electrode–electrolyte interaction.

The charge–discharge curves support, once again, the effect of CeO_2 on the electrochemical properties of layered oxides (Figure 6). To activate oxygen redox activity, the upper voltage limit is raised up to 4.5 V, just before the beginning of the electrode–electrolyte interaction. At a low charging rate (i.e., at C/20), the first specific capacity increases for all the oxides treated with CeO_2 : from 120, 100 and 170 mAh/g to 150, 205 and 210 mAh/g for CNNM, CNM16 and CNT16. This increase is spectacular for the Mg-substituted oxide (i.e., about two times). It is worth mentioning that CeO_2 is not electrochemically active in this voltage window: between 1.5 and 4.5 V, CeO_2 delivers a capacity of less than 1 mAh/g (Figure S2). The cycling stability is also impressive for this oxide: after 20 cycles at a rate of C/20, the cycling stability is 90% for CNM16 versus 68% and 56% for CNNM and CNT16. Among all oxides, the worst cycling stability is displayed by CNT16. It is interesting that the cycling stability resembles that of the metal-substituted oxides. Furthermore, the rate capability of CNM16 outperforms those of CNNM and CNT16. These data imply that CeO_2 provokes an increase in the specific capacity of layered oxides, while metal substituents control their cycling stability and rate capability.

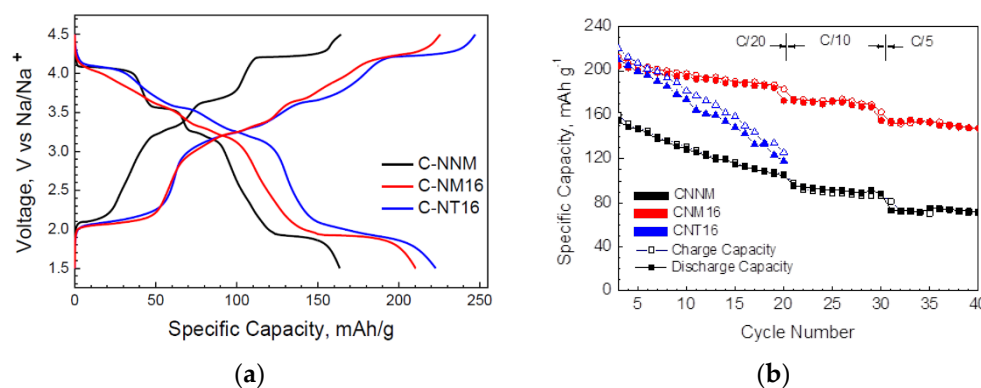


Figure 6. Charge–discharge curves after the 2nd cycle for CNNM, CNM16 and CNT16 in sodium-ion cells (a). Specific capacity, cycling stability and rate capability for CNNM, CNM16 and CNT16 in sodium-ion cells (b).

2.2.2. Lithium-Ion Cells

In addition to Na^+ , three-layered oxides are able to intercalate Li^+ too (Figure 7). In Li-ion cells, the OCV increases from Ti- to Mg-substituted oxides irrespective of the CeO_2 -treatment, which is another experimental sign of the alteration in the Ni oxidation state after metal substitution. It is worth mentioning that the OCV values of oxides in Li-ion cells are much more than that in Na-ion cells (i.e., exceed significantly 0.3 V corresponding to the difference in the standard potential of Li/Li^+ and Na/Na^+ , Figures 4 and 7). This is a consequence of the partial extraction of Na^+ and/or Li^+/Na^+ exchange induced by lithium electrolyte before the electrochemical reaction [31]. Thus, the first anodic scan in Li-ion cells embodies the extraction of the last Na^+ ions from the layered oxide (i.e., less resolved peaks between 3.0 and 4.0 V). Above 4.0 V, the CV curve of NNM is dominated by two intensive peaks at 4.17 and 4.65 V. The metal substitution leads to a smooth shift in the peak from 4.17 to 4.33 V following the order $\text{NNM} < \text{NM16} < \text{NT16}$. After the oxide treatment with CeO_2 , there is a slight lowering in the peak position, but the observed order remains unchanged: $\text{CNM} < \text{CNM16} < \text{CNT16}$. For all the oxides, this peak becomes more intensive after the Ti substitution and CeO_2 treatment. The next anodic peak at 4.65 V is

suppressed for the metal-substituted oxide and their CeO₂-treated analogues. After 4.8 V, the strong increase in the anodic current implies electrolyte decomposition, which is most pronounced for the Mg-substituted oxide.

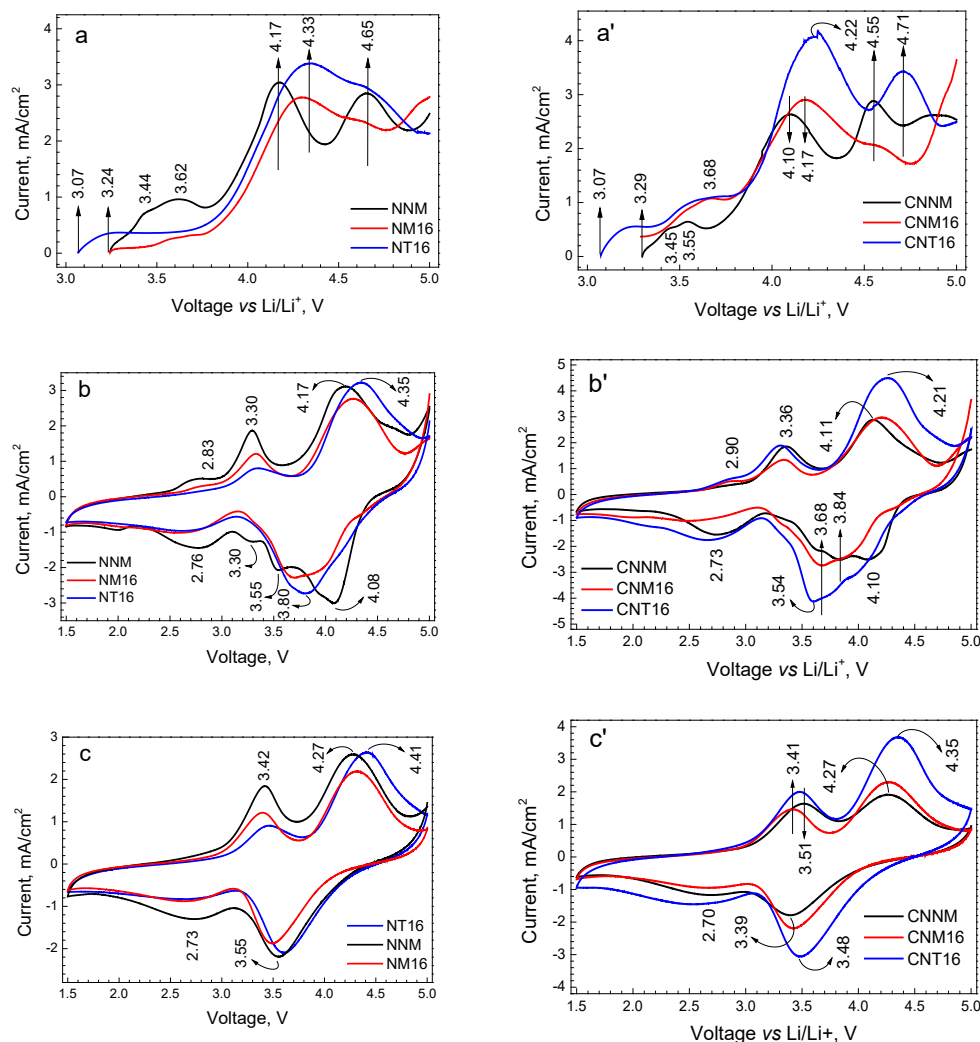


Figure 7. CV curves of metal-substituted oxides (a–c) and their CeO₂-treated analogues (a’–c’) in lithium-ion cells: (i) first anodic scan (a,a’); (ii) the corresponding cathodic scan and next anodic scan (b,b’); (iii) CV curves after five cycle (c,c’). The scan rate is 1 mV/s.

The reverse cathodic scan produces the appearance of several peaks between 4.1 and 2.0 V, some of them not being recovered during cell cycling. The stable CV curves are observed after five cycles. This behavior is valid for all the substituted and treated oxides. The CV curves consist of two redox peaks at 4.2 V/3.6 V and 3.4 V/2.7 V. The metal substituents and CeO₂ modifiers have an impact on the positions of these peaks, which is more pronounced for the high-voltage peak. The Ti⁴⁺ substituent leads to the strongest shift in the high-voltage peak, while for the Mg²⁺ substituent, the peak position is intermediate between those of NNM and NT16. The same picture is visible for the CeO₂-treated oxides.

The Mg²⁺/Ti⁴⁺ substituents and CeO₂ modifiers also affect the specific capacity, cycling stability and rate capability of layered oxides (Figure 8). The specific capacity of the substituted oxides increases following the order Mg²⁺ < Ti⁴⁺ (Figure 8). This order becomes inverted concerning the cycling stability: 72% for NNM, 81% for NM16 and 69% for NT16 at a rate of C/20. In accordance with the cycling stability, the rate capability is also better for the Mg²⁺-substituted oxides (Figure 8). The treatment of layered oxides with

CeO₂ leads to a strong increase in the specific capacity, as a result of which all the modified oxides deliver the close discharge capacities (i.e., about 170–190 mAh/g). It is important that the cycling stability and rate capability are also comparable for all the treated oxides and that they outperform those of the untreated oxides: the cycling stability is 77% for CNNM, 86% for CNM16 and 82% for CNT16 at a rate of C/20. At a rate of C/2 and a broad voltage window (i.e., between 1.5 and 4.8 V), the high capacity is delivered by CNT16 (i.e., around 150 mAh/h), while the cycling stability remains comparable for all the treated oxides (Figure 8). This confirms the good cycling stability of the treated oxides even in the extended voltage range, where the well-known Li-rich layered oxides failed [8].

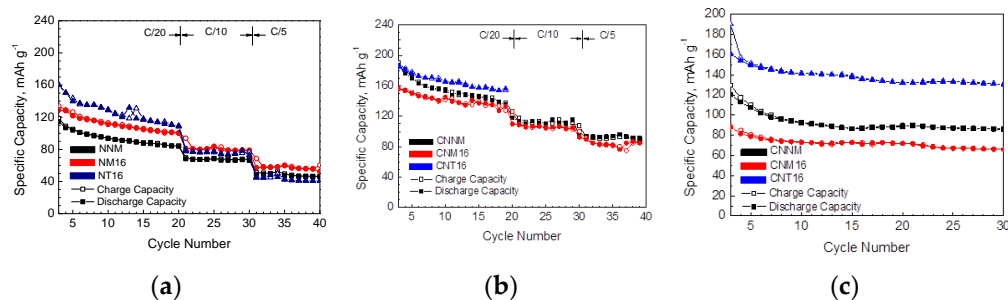


Figure 8. Specific capacity, cycling stability and rate capability for NNM, NM16 and NT16 (a) and their CeO₂-treated analogues CNNM, CNM16 and CNT16 (b) in lithium-ion cells worked between 1.5 and 4.5 V. The cycling stability for CNNM, CNM16 and CNT16 at a rate of C/2 between 1.5 and 4.8 V (c).

The electrochemical results reveal that, during Li⁺ intercalation into layered oxides, the Ti⁴⁺ and Mg²⁺ substituents amplify the oxygen redox activity to a lesser extent than the CeO₂ modifier does. In addition, the CeO₂-treated oxides demonstrate better cycling and rate capability.

2.3. Surface Deposition after Na⁺ and Li⁺ Intercalation

2.3.1. Sodium Electrolyte

The CV curves indicate that metal substituents and the CeO₂ modifier also influence the electrode–electrolyte interaction. The possible interaction is monitored by EPR spectroscopy, which allows simultaneously assessing the bulk and surface of electrodes (Figure 9). This is the main advantage of EPR spectroscopy over the surface XPS technique [31]. The EPR spectra of electrodes are dominated by the broad Lorentzian line due to the exchange of coupled nickel and manganese ions (Figure 9). Both the *g*-factor and EPR line width seem comparable with those for the pristine electrodes irrespective of the metal substituents or CeO₂ modifier: at 295 K, the *g*-factor is close to 2.0, and the EPR line width reaches the following values: 140 mT for pristine NNM versus 125 mT and 130 mT for NNM and CNNM electrodes; 105 mT for pristine NM16 versus 105 mT and 115 mT for NM16 and CNM16 electrodes; 130 mT for pristine NT16 versus 125 mT and 140 mT for NT16 and CNT16 electrodes. This is a clear indication that Ni–Mn spin systems in the bulk of the metal-substituted and CeO₂-treated oxides are preserved after electrode cycling.

The most important difference between pristine and cycled electrodes is the appearance of a hyperfine sextet signal with a *g*-factor of 2.0 and a hyperfine structure of 9.4 mT (Figure 9). The EPR parameters match those previously established for Mn²⁺ in MnF₂ (an average *g*-factor of 2.0017 and an average hyperfine structure of 9.17 mT) [39]. Based on this comparison, the sextet signal detected at oxide electrodes can be attributed to Mn²⁺ ions surrounded by F⁻ ions. The simultaneous appearance of the sextet and the main signal implies that the Mn²⁺–F⁻ complexes are magnetically isolated from the main Ni–Mn spin system, thus allowing locating them on the oxide surface. Mn²⁺–F⁻ complexes originate from the electrode–electrolyte interaction. It is well recognized that fluorine-based electrolytes attack the oxide electrode (especially at voltages higher than 4.2 V), leading to a series of reactions, including transition metal dissolution, surface reconstruction, surface deposition

of decomposed products (such as fluorides, carboxylates, carbonates, hydroxides, etc.), which, in turn, are responsible for capacity fading at layered oxides [40].

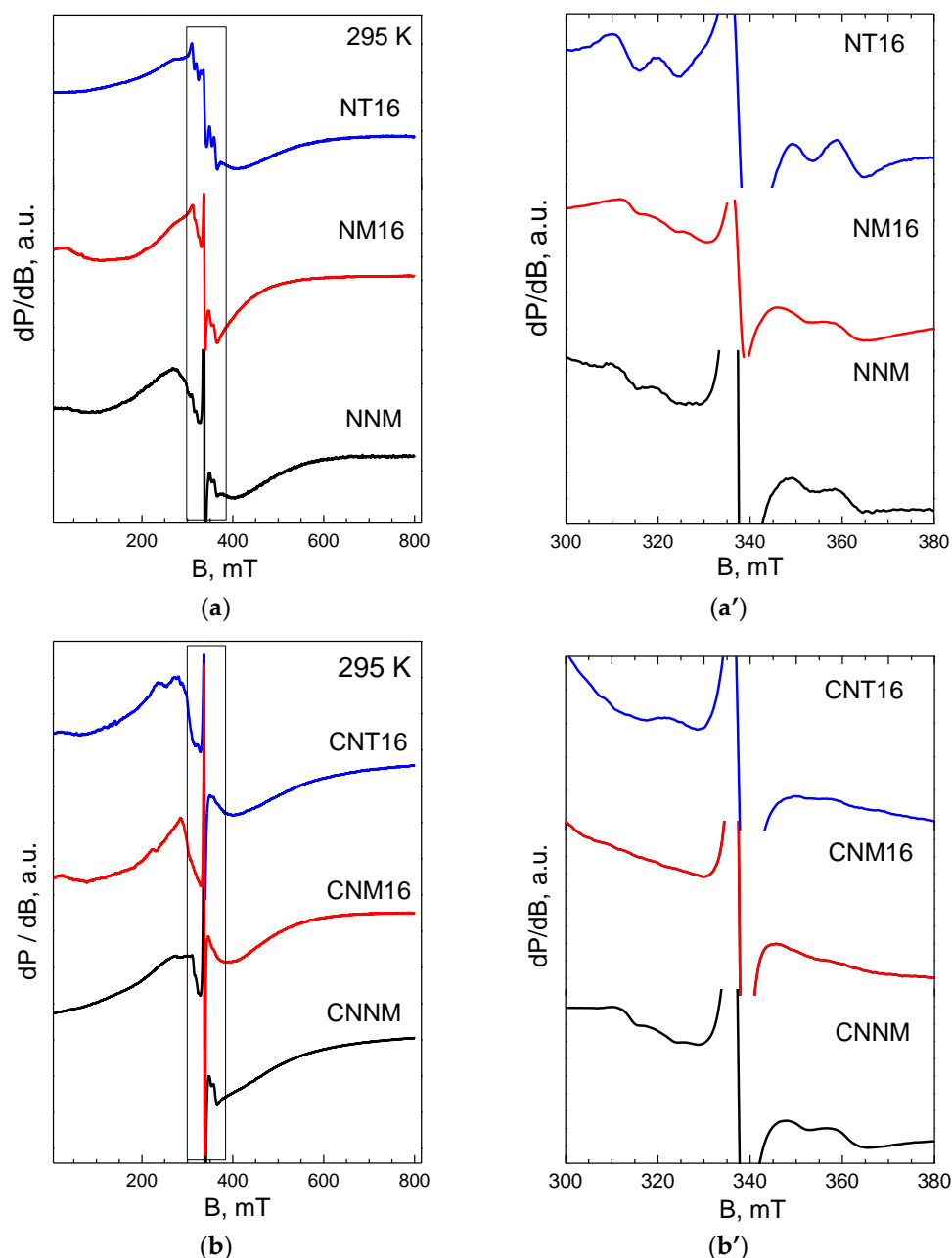


Figure 9. EPR spectra of metal-substituted oxides (a) and CeO_2 -treated analogues (b) after cycling in sodium-ion cells between 1.5 and 4.5 V for 40 times (the cell is switched off at 1.5 V). The parts of the spectra in the narrow range of the magnetic field (i.e., between 300 and 380 mT) are also shown (a',b').

Because of the hyperfine structure and high sensitivity towards Mn^{2+} ions, EPR spectroscopy enables detecting some of the surface manganese products, such as manganese fluorides, on the layered oxides. To quantify them, we used the relative intensity of the sextet signal. The relative intensity is highest for the Ti-substituted oxide and lowest for the Mg-substituted oxide (i.e., 0.7, 0.5 and 1.0 for NNM, NM16 and NT16). After treating oxides with CeO_2 , the sextet signal drastically decreases, and it becomes hardly visible: for CNNM, it is less than 0.2, while for CNM16 and CNT16, it is practically not detectable. This proves that the Ti^{4+} substituents favor the surface interaction of layered oxides with

NaPF₆-based electrolytes, leading to the deposition of MnF₂, while Mg²⁺ substituents and CeO₂ modifiers inhibit the surface deposition of MnF₂. It is interesting that the EPR data on electrode–electrolyte interactions correlate well with the electrochemical properties of oxides. The deposited MnF₂ seems to play a two-fold role: on the one hand, it passivates the electrode surface, thus preventing further interaction with electrolytes and their decomposition (illustrated by the dependence of the oxidation peak above 4.5 V on Mg²⁺, Ti⁴⁺ and CeO₂, Figures 3 and 6); on the other hand, it impedes the alkali ion transfer from the oxide surface into the bulk (illustrated by cycling stability and rate capability of Ti-substituted oxides, Figures 6 and 8).

Based on electrochemical and ex situ EPR experiments, it appears that CeO₂ has several impacts. First, CeO₂ amplifies the peak due to oxygen redox activity; second, CeO₂ shifts the high-voltage peak down due to the electrode–electrolyte interaction; third, CeO₂ suppresses the deposition of MnF₂ on the electrode surface. It is worth mentioning that, in fuel cells with polymer electrolyte membranes, non-stoichiometric CeO_{2- δ} significantly improves the chemical stability of the membrane due to its ability to scavenge the in situ generated oxygen radicals [41]. At this level of study, there are no observations of CeO₂'s possible impact on the decomposition of sodium electrolytes comprising 1 M NaPF₆ solution in propylene carbonate. However, through the DFT study, it has been demonstrated that propylene carbonate undergoes oxidative decomposition with a formation of acetone radical and CO₂ as the primary product [42]. That is why it is not possible to reject CeO₂ modifiers operating as free-radical scavengers in sodium electrolytes.

2.3.2. Lithium Electrolyte

The EPR signals due to the oxide bulk and surface are also observed after the cycling of electrodes in lithium-ion cells instead of sodium ones (Figure 10). The bulk EPR signal undergoes more significant broadening during the lithium intercalation than that of sodium (Figure 9) [35,43]. The line broadening reflects the transformation from the P3 structure into the O3 structure, where a partial exchange between Li⁺ from lithium layers with Ni²⁺ ions of transition metal layers takes place. The comparison of the EPR spectra shows that Ti⁴⁺ ions and CeO₂ modifier cause stronger line broadening than that of Mg²⁺. This can be related to higher capacities delivered by Ti-substituted and CeO₂-modified oxides.

The surface sextet signal due to deposited MnF₂ is also visible for oxide electrodes cycled in lithium-ion cells. The relative intensity of this signal is highest for the Ti-substituted oxide and lowest for the Mg-substituted oxide: 0.8, 0.5 and 1.0 for NNM, NM16 and NT16. After the oxide modification with CeO₂, the sextet signal almost vanished (Figure 10). It is noticeable that the same order in the intensity variation is established for oxides cycled in sodium-ion cells. On the one hand, this reveals that LiPF₆- and NaPF₆-based electrolytes interact in the same way with oxide electrodes, resulting in MnF₂ deposition. On the other hand, the interaction is modulated by metal substituents and CeO₂; it is intensified by the Ti⁴⁺ ions and hindered by the Mg²⁺ ions and CeO₂ modifier. The hindrance at MnF₂ deposition facilitates, on one hand, the interaction between the oxide electrolyte and the electrolyte but, on the other hand, mitigates the alkali ions transfer from the oxide surface into the bulk. As a result, the CeO₂-modified oxides display a better electrochemical performance both in sodium and lithium-ion cells.

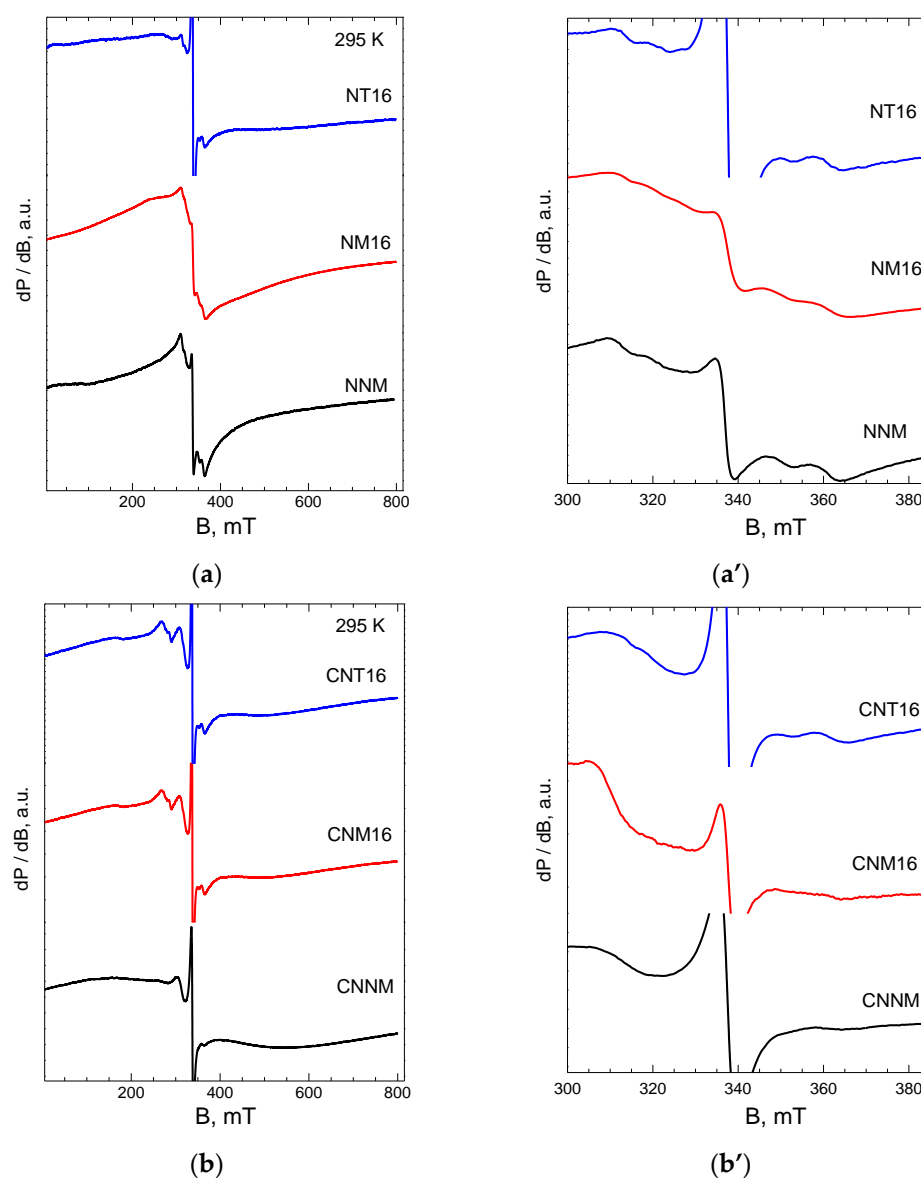


Figure 10. EPR spectra of metal-substituted oxides (a,a') and CeO₂-treated oxides (b,b') after cycling in lithium-ion cells. The right figures present the EPR spectra in the narrow range of the magnetic field. The parts of the spectra in the narrow range of magnetic field (i.e., between 300 and 385 mT) are also shown (a',b').

3. Materials and Methods

3.1. Materials

Depending on the kind of metal substituents, two synthetic procedures were carried out. The Mg-substituted oxide, Na_{2/3}Ni_{1/3}Mg_{1/6}Mn_{1/2}O₂, is obtained by freeze-drying aqueous solutions containing acetate salts of Na⁺, Ni²⁺, Mg²⁺ and Mn²⁺ ions, followed by thermal decomposition at 400 °C. The solid residues were ground, pelleted and annealed at 700 °C for 24 h. The details are given elsewhere [33].

The synthesis of Ti-substituted oxides is based on Pechini's method. The initial reagents comprise nickel and manganese acetates, sodium nitrate, TiO₂ (anatase type, ≥99%, Honeywell Fluka, Mecklenburg, NC, USA), citric acid and ethylene glycol. The synthetic method includes several steps. First, the acetate solution of nickel and manganese is prepared. Then, TiO₂, citric acid and, finally, a nitrate solution of sodium are added sequentially to the acetate solution. The suspension is heated at 90 °C under vigorous stirring. The solution of ethylene glycol is slowly added to the suspension, and heating

continued until a thick gel forms, followed by the decomposition of the gel at 400 °C in air. The decomposed products are treated in the same way as the magnesium-substituted oxides. For the sake of convenience, the unsubstituted and metal-substituted oxides will be denoted as NNM, NM16 and NT16, respectively.

The treatment of layered oxides with CeO₂ is accomplished by impregnating NNM, NM16 and NT16 with an aqueous solution of cerium acetate (Cerium(III) acetate hydrate, 99.9% trace metals basis, Sigma Aldrich, St. Louis, MO, USA). The amount of cerium acetate is calculated to obtain 5 wt.% CeO₂ in the target compound. The impregnated oxides are annealed at 700 °C for 2 h in an oxygen atmosphere. The treated oxides will be denoted as CNNM, CNM16 and CNT16, respectively.

3.2. Methods

The structure of oxides was determined by powder X-ray diffraction using the Bruker Advance D8 powder diffractometer with CuK α radiation (Germany). The TEM analysis was carried out on a JEOL 2100 microscope. The specimens were prepared in acetone by ultrasonic treatment. The suspensions were then dripped on standard holey carbon/Cu grids. The HR-TEM images were quantified by Digital Micrograph software. The EPR spectra were collected on a Bruker EMX^{plus} spectrometer (Germany) within the temperature range of 100–400 K. The specific surface area of oxides varies between 1 and 3 m²/g without any clear dependence on the number of metal substituents and CeO₂ modifiers.

The electrodes were fabricated by mixing the active material with carbon black (Super C65) and polyvinylidene fluoride (PVDF) in N-methyl-2-pyrrolidone at a dry weight ratio of 80:10:10. The slurry was cast on aluminum foil, followed by drying at 80 °C overnight. The disk electrodes with a diameter of 9 mm were cut, pressed and dried at 120 °C under vacuum. The mass loading of active material was 3.50 ± 0.5 mg.cm⁻². The Swagelok-type cells were mounted in a glovebox (MBraun, MB-Unilab Pro SP (1500/780), H₂O, and O₂ content <0.1 ppm). The counter electrode consisted of clean lithium or sodium metal. As electrolytes, we applied 1 M LiPF₆ in EC/DMC and 1M NaPF₆ in PC. The separator comprises a Whatman GF/D glass microfiber layer. The cell testing was carried out using an Arbin battery cyler (Series LBT20084) in galvanostatic mode. The CV experiments were performed on Autolab PGStat 204 potentiostat. Each electrochemical experiment was repeated at least twice, showing a rather high reproducibility.

The ex situ EPR experiments were performed on the electrodes recovered from cells cycled 40 times between 1.5 and 4.5 V and switched off at 1.5 V. The electrochemical cells were disassembled inside the glovebox, and the recovered electrodes were subjected to a washing step with dimethyl carbonate (DMC) to eliminate electrolyte residues. The EPR quartz tube was filled with recovered electrodes inside the glovebox.

4. Conclusions

The morphology and electrochemical properties of P3-Na_{2/3}Ni_{1/2}Mn_{1/2}O₂ were effectively modified by Mg²⁺ and Ti⁴⁺ substitution complemented with CeO₂ treatment. The incorporation of Mg²⁺ and Ti⁴⁺ ions into the layered structure of Na_{2/3}Ni_{1/2}Mn_{1/2}O₂ is accomplished through a selective replacement of low- and high-oxidized nickel ions, respectively. The impregnation of metal-substituted oxides with a small amount of cerium acetate leads to the formation of two-phase composites between layered oxide and CeO₂, in which the layered structure remains intact, and the particle distribution becomes more homogeneous.

The Ti⁴⁺ substituents amplify the oxygen redox activity during Na⁺ and Li⁺ intercalation, thus permitting reaching the highest specific capacity at potentials above 4.2 V. At the same time, the interaction of oxides with NaPF₆- and LiPF₆-based electrolytes is intensified, leading to a deposition of MnF₂. As a result, Ti-substituted oxide displays moderate cycling stability and poor rate capability. Contrary to Ti⁴⁺, the Mg²⁺ substituents mainly influence the nickel redox activity and suppress the deposition of MnF₂, all of them contributing to the exceptional cycling stability and rate capability. The CeO₂ modifier has a much stronger

effect on the oxygen redox activity than that of metal substituents; thus, the highest specific capacity is attained. In addition, the CeO₂ modifier tunes the electrode–electrode interaction by eliminating the deposition of MnF₂.

By combining the appropriate substituents with the CeO₂ modifier, the best electrode material was selected. For Na-ion cells, this is the Mg-substituted oxide modified with CeO₂, which displays high capacity, excellent cycling stability and exceptional rate capability. For Li-ion cells, the Ti-substituted oxide modified by CeO₂ display the best performance.

This study demonstrates that the oxygen redox activity of three-layered oxides can be regulated by a rational combination of metal substituents and oxygen storage modifiers. Although the CeO₂ modifier provokes an increase in the specific capacity of layered oxides, the metal substituents control their cycling stability and rate capability. We think that the proposed oxide architecture that includes target metal substituents and oxygen-storage modifiers may open up new directions for the elaboration of electrode materials with colossal intercalation capacity and designed for both Li- and Na-ion batteries.

Supplementary Materials: The following supporting information can be downloaded at: <https://www.mdpi.com/article/10.3390/batteries8060056/s1>, Figure S1: XRD patterns of NNM, NM-16, NT-16 and their CeO₂-treated analogues. Figure S2: Charge–discharge curves of CeO₂ in a sodium-ion cell.

Author Contributions: Conceptualization, R.S. and M.K.; methodology, E.Z. and R.S.; software, M.K. and R.K.; validation, M.K. and R.K.; investigation, M.K. and R.K.; resources, R.S.; data curation, M.K.; writing—original draft preparation, R.S. and M.K.; writing—review and editing, E.Z. and R.S.; visualization, M.K. and R.K.; project administration, R.S.; funding acquisition, R.S. All authors have read and agreed to the published version of the manuscript.

Funding: This research was funded by the Bulgarian National Science Fund, grant number contract CARiM (NSP Vihren, KII-06-ДБ-6).

Institutional Review Board Statement: Not applicable.

Informed Consent Statement: Not applicable.

Data Availability Statement: Not applicable.

Acknowledgments: The authors acknowledge the financial support of the Bulgarian National Science Fund, contract CARiM (NSP Vihren, KII-06-ДБ-6). The MBRAUN glovebox was used within the framework of the National Center of Mechatronics and Clean Technologies (BG05M2OP001-1.001-0008). The authors are grateful to Diana Nihtianova for the TEM analysis.

Conflicts of Interest: The authors declare no conflict of interest.

References

1. Gür, T.M. Review of electrical energy storage technologies, materials and systems: Challenges and prospects for large-scale grid storage. *Energy Environ. Sci.* **2018**, *11*, 2696–2767. [[CrossRef](#)]
2. Whittingham, M.S. Special editorial perspective: Beyond Li-ion battery chemistry. *Chem. Rev.* **2020**, *120*, 6328–6330. [[CrossRef](#)] [[PubMed](#)]
3. Abraham, K.M. How comparable are sodium-ion batteries to lithium-ion counterparts? *ACS Energy Lett.* **2020**, *5*, 3544–3547. [[CrossRef](#)]
4. Rahman, M.M.; Lin, F. Oxygen redox chemistry in rechargeable Li-ion and Na-ion batteries. *Matter* **2021**, *4*, 490–527. [[CrossRef](#)]
5. Lee, G.; Lau, V.W.; Yang, W.; Kang, Y. Utilizing oxygen redox in layered cathode materials from multiscale perspective. *Adv. Energy Mater.* **2021**, *11*, 2003227. [[CrossRef](#)]
6. Delmas, C. Sodium and sodium-ion batteries: 50 years of research. *Adv. Energy Mater.* **2018**, *8*, 1703137. [[CrossRef](#)]
7. Koga, H.; Croguennec, L.; Ménétrier, M.; Mannesiez, P.; Weill, F.; Delmas, C. Different oxygen redox participation for bulk and surface: A possible global explanation for the cycling mechanism of Li_{1.20}Mn_{0.54}Co_{0.13}Ni_{0.13}O₂. *J. Power Sources* **2013**, *236*, 250–258. [[CrossRef](#)]
8. He, W.; Guo, W.; Wu, H.; Lin, L.; Liu, Q.; Han, X.; Xie, Q.; Liu, P.; Zheng, H.; Wang, L.; et al. Challenges and recent advances in high capacity Li-rich cathode materials for high energy density lithium-ion batteries. *Adv. Mater.* **2021**, *33*, 2005937. [[CrossRef](#)]
9. De La Llave, E.; Talaie, E.; Levi, E.; Nayak, P.K.; Dixit, M.; Rao, P.T.; Hartmann, P.; Chesneau, F.; Major, D.T.; Greenstein, M.; et al. Improving Energy Density and Structural Stability of Manganese Oxide Cathodes for Na-Ion Batteries by Structural Lithium Substitution. *Chem. Mater.* **2016**, *28*, 9064–9076. [[CrossRef](#)]

10. Ma, C.; Alvarado, J.; Xu, J.; Clément, R.J.; Kodur, M.; Tong, W.; Grey, C.P.; Meng, Y.S. Exploring oxygen activity in the high energy P2-type $\text{Na}_{0.78}\text{Ni}_{0.23}\text{Mn}_{0.69}\text{O}_2$ cathode material for Na-ion batteries. *J. Am. Chem. Soc.* **2017**, *139*, 4835–4845. [[CrossRef](#)]
11. Maitra, U.; House, R.A.; Somerville, J.W.; Tapia-Ruiz, N.; Lozano, J.G.; Guerrini, N.; Hao, R.; Luo, K.; Jin, L.; Pérez-Osorio, M.A.; et al. Oxygen redox chemistry without excess alkali-metal ions in $\text{Na}_{2/3}[\text{Mg}_{0.28}\text{Mn}_{0.72}]\text{O}_2$. *Nat. Chem.* **2018**, *10*, 288–295. [[CrossRef](#)] [[PubMed](#)]
12. Bai, X.; Sathiya, M.; Mendoza-Sánchez, B.; Iadecola, A.; Vergnet, J.; Dedryvère, R.; Saubanère, M.; Abakumov, A.M.; Rozier, P.; Tarascon, J.M. Anionic redox activity in a newly Zn-doped sodium layered oxide $\text{P2-Na}_{2/3}\text{Mn}_{1-y}\text{Zn}_y\text{O}_2$ ($0 < y < 0.23$). *Adv. Energy Mater.* **2018**, *8*, 1802379.
13. Wang, Y.; Kim, S.; Lu, J.; Feng, G.; Li, X. A study of Cu doping effects in $\text{P2-Na}_{0.75}\text{Mn}_{0.6}\text{Fe}_{0.2}(\text{Cu}_x\text{Ni}_{0.2-x})\text{O}_2$ layered cathodes for sodium-ion batteries. *Batter. Supercaps* **2020**, *3*, 376–387. [[CrossRef](#)]
14. Zhao, C.; Yao, Z.; Wang, J.; Lu, Y.; Bai, X.; Aspuru-Guzik, A.; Chen, L.; Hu, Y.-S. Ti Substitution facilitating oxygen oxidation in $\text{Na}_{2/3}\text{Mg}_{1/3}\text{Ti}_{1/6}\text{Mn}_{1/2}\text{O}_2$ cathode. *Chem.* **2019**, *5*, 2913–2925. [[CrossRef](#)]
15. Mortemard de Boisse, B.; Nishimura, S.-I.; Watanabe, E.; Lander, L.; Tsuchimoto, A.; Kikkawa, J.; Kobayashi, E.; Asakura, D.; Okubo, M.; Yamada, A. Highly reversible oxygen-redox chemistry at 4.1 V in $\text{Na}_{4/7-x}[\square_{1/7}\text{Mn}_{6/7}]\text{O}_2$ (\square : Mn vacancy). *Adv. Energy Mater.* **2018**, *8*, 1800409. [[CrossRef](#)]
16. Kubota, K.; Komaba, S. Review-practical issues and future perspective for Na-ion batteries. *J. Electrochem. Soc.* **2015**, *162*, A2538–A2550. [[CrossRef](#)]
17. Xu, J.; Sun, M.; Qiao, R.; Renfrew, S.; Ma, L.; Wu, T.; Hwang, S.; Nordlund, D.; Su, D.; Amine, K.; et al. Elucidating anionic oxygen activity in lithium-rich layered oxides. *Nat. Commun.* **2018**, *9*, 947. [[CrossRef](#)]
18. Lee, J.; Papp, J.K.; Clément, R.J.; Sallis, S.; Kwon, D.-H.; Shi, T.; Yang, W.; McCloskey, B.; Ceder, G. Mitigating oxygen loss to improve the cycling performance of high capacity cation-disordered cathode materials. *Nat. Commun.* **2017**, *8*, 981. [[CrossRef](#)]
19. Zhou, K.; Zheng, S.; Ren, F.; Wu, J.; Liu, H.; Luo, M.; Liu, X.; Xiang, Y.; Zhang, C.; Yang, W.; et al. Fluorination effect for stabilizing cationic and anionic redox activities in cation-disordered cathode materials. *Energy Storage Mater.* **2020**, *32*, 234–243. [[CrossRef](#)]
20. Li, Z.; Kong, W.; Yu, Y.; Zhang, J.; Wong, D.; Xu, Z.; Chen, Z.; Schulz, C.; Bartkowiak, M.; Liu, X. Tuning bulk O_2 and nonbonding oxygen state for reversible anionic redox chemistry in P2-layered cathodes. *Angew. Chem. Int. Ed. Engl.* **2022**, *134*, e202115552.
21. Kaur, G.; Gates, B.D. Review—Surface coatings for cathodes in lithium ion batteries: From crystal structures to electro-chemical performance. *J. Electrochem. Soc.* **2022**, *169*, 043504. [[CrossRef](#)]
22. Nisar, U.; Muralidharan, N.; Essehli, R.; Amin, R.; Belharouak, I. Valuation of surface coatings in high-energy density lithium-ion battery cathode materials. *Energy Storage Mater.* **2021**, *38*, 309–328. [[CrossRef](#)]
23. Shi, C.; Wang, L.; Chen, X.; Wang, S.; Wang, J.; Jin, H. Challenges of layer-structured cathodes for sodium-ion batteries. *Nanoscale Horiz.* **2022**, *7*, 338–351. [[CrossRef](#)] [[PubMed](#)]
24. Hwang, J.-Y.; Myung, S.-T.; Choi, J.U.; Yoon, C.S.; Yashiro, H.; Sun, Y.-K. Resolving the degradation pathways of the O_3 -type layered oxide cathode surface through the nano-scale aluminum oxide coating for high-energy density sodium-ion batteries. *J. Mater. Chem. A* **2017**, *5*, 23671–23680. [[CrossRef](#)]
25. Wang, Y.; Tang, K.; Li, X.; Yu, R.; Zhang, X.; Huang, Y.; Chen, G.; Jamil, S.; Cao, S.; Xie, X.; et al. Improved cycle and air stability of $\text{P3-Na}_{0.65}\text{Mn}_{0.75}\text{Ni}_{0.25}\text{O}_2$ electrode for sodium-ion batteries coated with metal phosphates. *Chem. Eng. J.* **2019**, *372*, 1066–1076. [[CrossRef](#)]
26. Yu, Y.; Kong, W.; Li, Q.; Ning, D.; Schuck, G.; Schumacher, G.; Su, C.; Liu, X. Understanding the multiple effect of TiO_2 coating on $\text{NaMn}_{0.33}\text{Fe}_{0.33}\text{Ni}_{0.33}\text{O}_2$ cathode material for Na-ion batteries. *ACS Appl. Energy Mater.* **2020**, *3*, 933–942. [[CrossRef](#)]
27. House, R.A.; Maitra, U.; Jin, L.; Lozano, J.G.; Somerville, J.W.; Rees, N.H.; Naylor, A.J.; Duda, L.C.; Massel, F.; Chadwick, A.V.; et al. What triggers oxygen loss in oxygen redox cathode materials? *Chem. Mater.* **2019**, *31*, 3293–3300. [[CrossRef](#)]
28. Chen, Q.; Pei, Y.; Chen, H.; Song, Y.; Zhen, L.; Xu, C.-Y.; Xiao, P.; Henkelman, G. Highly reversible oxygen redox in layered compounds enabled by surface polyanions. *Nat. Commun.* **2020**, *11*, 3411. [[CrossRef](#)]
29. Hwang, J.-Y.; Yu, T.-Y.; Sun, Y.-K. Simultaneous MgO coating and Mg doping of $\text{NaNi}_{0.5}\text{Mn}_{0.5}\text{O}_2$ cathode: Facile and customizable approach to high-voltage sodium-ion batteries. *J. Mater. Chem. A* **2018**, *6*, 16854–16862. [[CrossRef](#)]
30. Shin, Y.; Kan, W.H.; Aykol, M.; Papp, J.K.; McCloskey, B.D.; Chen, G.; Persson, K.A. Alleviating oxygen evolution from Li-excess oxide materials through theory-guided surface protection. *Nat. Commun.* **2018**, *9*, 4597. [[CrossRef](#)]
31. Kalapsazova, M.L.; Kostov, K.L.; Kukeva, R.R.; Zhecheva, E.N.; Stoyanova, R.K. Oxygen-storage materials to stabilize the oxygen redox activity of three-layered sodium transition metal oxides. *J. Phys. Chem. Lett.* **2021**, *12*, 7804–7811. [[CrossRef](#)] [[PubMed](#)]
32. Song, B.; Hu, E.; Liu, J.; Zhang, Y.; Yang, X.-Q.; Nanda, J.; Huq, A.; Page, K. A novel P3-type $\text{Na}_{2/3}\text{Mg}_{1/3}\text{Mn}_{2/3}\text{O}_2$ as high capacity sodium-ion cathode using reversible oxygen redox. *J. Mater. Chem. A* **2019**, *7*, 1491–1498. [[CrossRef](#)]
33. Kalapsazova, M.; Markov, P.; Kostov, K.; Zhecheva, E.; Nihtianova, D.; Stoyanova, R. Controlling at elevated temperature the sodium intercalation capacity and rate capability of $\text{P3-Na}_{2/3}\text{Ni}_{1/2}\text{Mn}_{1/2}\text{O}_2$ through the selective substitution of nickel with magnesium. *Batter. Supercaps* **2020**, *3*, 1329–1340. [[CrossRef](#)]
34. Lee, J.; Koo, S.; Lee, J.; Kim, D. Rational design of Ti-based oxygen redox layered oxides for advanced sodium-ion batteries. *J. Mater. Chem. A* **2021**, *9*, 11762–11770. [[CrossRef](#)]
35. Yang, J.; Maughan, A.E.; Teeter, G.; de Villiers, B.J.T.; Bak, S.; Han, S. Structural stabilization of P2-type sodium iron manganese oxides by electrochemically inactive Mg substitution: Insights of redox behavior and voltage decay. *ChemSusChem* **2020**, *13*, 5972–5982. [[CrossRef](#)] [[PubMed](#)]

36. Stansby, J.H.; Sharma, N.; Goonetilleke, D. Probing the charged state of layered positive electrodes in sodium-ion batteries: Reaction pathways, stability and opportunities. *J. Mater. Chem. A* **2020**, *8*, 24833–24867. [[CrossRef](#)]
37. Zhu, Y.-F.; Xiao, Y.; Dou, S.-X.; Chou, S.-L. Dynamic structural evolution and controllable redox potential for abnormal high-voltage sodium layered oxide cathodes. *Cell Rep. Phys. Sci.* **2021**, *2*, 100631. [[CrossRef](#)]
38. Zhang, J.; Wang, W.; Wang, W.; Wang, S.; Li, B. Comprehensive review of P2-type $\text{Na}_{2/3}\text{Ni}_{1/3}\text{Mn}_{2/3}\text{O}_2$, a potential cathode for practical application of Na-ion batteries. *ACS Appl. Mater. Interfaces* **2019**, *11*, 22051–22066. [[CrossRef](#)]
39. Yosida, T.; Aoki, H.; Takeuchi, H.; Arakawa, M.; Horai, K. EPR, ^{19}F -ENDOR and ^{55}Mn -ENDOR of Mn^{2+} impurity center in MgF_2 single crystal. *J. Phys. Soc. Jpn.* **1991**, *60*, 625–635. [[CrossRef](#)]
40. Huang, Y.; Zhao, L.; Li, L.; Xie, M.; Wu, F.; Chen, R. Electrolytes and electrolyte/electrode interfaces in sodium-ion batteries: From scientific research to practical application. *Adv. Mater.* **2019**, *31*, e1808393. [[CrossRef](#)]
41. Kumar, A.; Hong, J.; Yun, Y.; Bhardwaja, A.; Song, S.-J. The role of surface lattice defects of $\text{CeO}_{2-\delta}$ nanoparticles as a scav-enging redox catalyst in polymer electrolyte membrane fuel cells. *J. Mater. Chem. A* **2020**, *8*, 26023–26034. [[CrossRef](#)]
42. Leggesse, E.G.; Lin, R.T.; Teng, T.-F.; Chen, C.-L.; Jiang, J.-C. Oxidative decomposition of propylene carbonate in lithium ion batteries: A DFT study. *J. Phys. Chem. A* **2013**, *117*, 7959–7969. [[CrossRef](#)] [[PubMed](#)]
43. Kalapsazova, M.; Kostov, K.; Zhecheva, E.; Stoyanova, R. Hybrid Li/Na ion batteries: Temperature-induced reactivity of three-layered oxide ($\text{P3-Na}_{2/3}\text{Ni}_{1/3}\text{Mg}_{1/6}\text{Mn}_{1/2}\text{O}_2$) toward lithium ionic liquid electrolytes. *Front. Chem.* **2020**, *8*, 600140. [[CrossRef](#)] [[PubMed](#)]